

# Non-parabolicity, band gap re-normalisation and carrier scattering in Si doped ZnO

R. E. Treharne<sup>a,\*</sup>, L. J. Phillips<sup>a</sup>, K. Durose<sup>a</sup>, A. D. Weerakkody<sup>b</sup>, I. Z. Mitrovic<sup>b</sup>, S. Hall<sup>b</sup>

<sup>a</sup>*Stephenson Institute for Renewable Energy, University of Liverpool, UK*

<sup>b</sup>*Department of Electrical Eng. and Electronics, University of Liverpool, UK*

---

## Abstract

A combinatorial methodology, developed for the rapid optimisation of sputtered transparent conducting oxides, is applied to Si doped ZnO. A wide range of compositions are explored over a single sample to determine an optimum composition, with respect to the minimisation of resistivity, of  $x = 0.65\%$  wt. SiO<sub>2</sub>. A fundamental investigation of the conduction band non-parabolicity yields values of  $m_{e0} = 0.35m_0$  and  $C = 0.3 \text{ eV}^{-1}$  for the conduction band minimum effective mass and the non-parabolicity factor respectively. Further analysis of extracted band gap values with respect to dopant concentration provides an estimate of the magnitude of re-normalization effects. Finally, a model is proposed to describe the carrier transport behaviour for a degenerate polycrystalline semiconductor by accounting for the tunnelling of carriers through grain boundaries.

*Keywords:* zinc oxide, magnetron sputtering, thin-film, doping, non-parabolicity, band gap normalisation

---

---

\*Corresponding author

Email address: [R.Treharne@liverpool.ac.uk](mailto:R.Treharne@liverpool.ac.uk) (R. E. Treharne)

## 1. Introduction

Polycrystalline ZnO films have received significant attention in recent years. They can be degenerately doped, typically by incorporating group III (e.g. Al, Ga or In [1]) or group VII (e.g. F [2, 3], Cl [4]) elements to achieve resistivities of the order  $10^{-4} \Omega\text{cm}$ , while maintaining a high optical transparency ( $> 80\%$ ). Such ZnO based transparent conducting oxide (TCO) films, most notably Al doped ZnO (AZO), are now used extensively within thin-film photovoltaic technologies (namely CIGS, CZTS and CdTe) and have widely replaced the use of indium based TCOs. A wide range of deposition techniques has been demonstrated for ZnO films including atomic layer deposition (ALD) [5], metal-organic chemical vapour deposition (MOCVD) [6], pulsed laser deposition (PLD) [7] and magnetron sputtering [1, 8, 9].

The key property of a TCO is its resistivity, which in the context of thin-film PV, should be as low as possible. Film transmittance will generally remain high over the visible wavelength range for a wide range of resistivities, except in the case of exceptionally high free carrier concentrations (i.e.  $> 10^{21} \text{ cm}^{-3}$ ), and so is of secondary concern experimentally. The most common approach to minimising a TCO's resistivity is to generate large sample sets over which a single experimental parameter (e.g. pressure, temperature, composition) is varied incrementally. Such investigations are time consuming and the experimental consistency from sample to sample can be poor due to uncontrollable drifts in other associated deposition parameters. Furthermore, even for large sample sets the relationship determined between the resultant film properties and the deposition conditions can often be ambiguous. This is particularly true for resistivity which is highly sensitive and can vary on the scale of several orders of magnitude for a very narrow range of composition.

In this work, a combinatorial methodology is developed for the study of TCO materials and demonstrated in the case Si doped ZnO (SZO). The approach eliminates the need for large sample sets and generates results that are highly consistent and reliable. We demonstrate how the methodology can be

used to investigate fundamental properties of the material, namely conduction band non-parabolicity and band gap re-normalization, as well as more empirical relationships such as the compositional dependence of electrical properties. Furthermore, the consideration of a grain boundary limited scattering mechanism to describe the observed transport behaviour in SZO leads to the proposal of an extension to the current theory to apply in the case of degenerately doped polycrystalline films.

## 2. Experimental Methods

Films were deposited via RF magnetron sputtering using an AJA Phase II-J Orion system. The system was configured in a ‘sputter-up’ geometry with the substrate being suspended above two separate ceramic targets of ZnO and SiO<sub>2</sub> arranged off-centre and tilted at 5° towards the centre of the substrate. Soda-lime glass substrates (OptiWhite<sup>TM</sup>, NSG Pilkington) of size 100 × 100 × 4 mm<sup>3</sup> were cleaned by scrubbing with a nylon brush and a series of de-ionized water and isopropanol alcohol rinses followed by blow drying with a nitrogen gas jet. During deposition the ZnO and SiO<sub>2</sub> targets were sputtered simultaneously using powers of 150 W and 50 W respectively. A growth pressure of  $2.7 \times 10^{-3}$  mbar Ar was used during deposition. The substrate temperature was maintained at  $350 \pm 5^\circ\text{C}$  during growth and the substrate was kept static with respect to the magnetrons (i.e the substrate was not rotated). Deliberate gradients of both thickness and composition were therefore incorporated across the resultant film to generate a ‘combinatorial’ sample. A second film of pure SiO<sub>2</sub> was deposited under identical conditions (but without ZnO) to generate a reference film for estimating the % wt. profile of SiO<sub>2</sub> in the co-sputtered combinatorial sample.

A Shimadzu UV-Vis-IR 3700 spectrophotometer with mapping capability was used to measure the transmittance of the co-sputtered film over the range 250 - 2500 nm. 289 spectra were taken in total at 5 mm increments over the full sample surface. At each of these 289 points the sheet resistance was also measured using a CMT-SR2000 4-point probe mapping system. Following transmit-

60 tance and sheet resistance measurements the sample was cut into one hundred  
 61  $10 \times 10 \text{ mm}^2$  pieces. A selection of these pieces, 10 in total, were further scribed  
 62 into four  $5 \times 5 \text{ mm}^2$  sections and Hall measurement were performed on each  
 63 of these sections. Hall measurements were performed with custom built equip-  
 64 ment, provided by Semimetrics Ltd., using a field strength of 0.8 T. Ellipsometry  
 65 was performed on the same sections using a Woollam M2000-UI system. Ellip-  
 66 sometry was also used to map the thickness profile of the pure  $\text{SiO}_2$  reference  
 67 film.

### 68 **3. Results**

#### 69 *3.1. Fitting of optical spectra*

70 Figure 1 shows a typical transmittance spectra taken from a single point  
 71 on the combinatorial ZnO:Si sample and the corresponding fit achieved using  
 72 a theoretical model of the material's dielectric permittivity  $\varepsilon(\omega)$ . Full details  
 73 of this model are given in [10]. The key components of the model include:  
 74 1) a Lorentzian oscillator to account for the behaviour of the system's bound  
 75 electrons and to provide a smoothly varying dielectric background over the range  
 76 of interest (250–2500 nm), 2) an extended Drude model [11], to characterise the  
 77 system's free electron response, and 3) an inter-band transition model to account  
 78 for the steep increase in the material's absorption coefficient in the vicinity of  
 79 its direct band gap (3.3–3.4 eV). The two key parameters extractable from the  
 80 dielectric model are the film's thickness,  $d$ , and plasma frequency,  $\omega_p$ , which is  
 81 related directly to the carrier concentration according to

$$\omega_p = \sqrt{\frac{n_e e^2}{m_e \varepsilon_\infty \varepsilon_0}} \quad (1)$$

82 where  $m_e$  is the effective electrons (expressed in units of the free electron mass,  
 83  $m_0$ ),  $\varepsilon_\infty$  is the material's high frequency relativity permittivity ( $\sim 8.3$  for single  
 84 crystal ZnO [12]) and  $\varepsilon_0$  is the permittivity of free space. Note that as  $\varepsilon_\infty$  is not  
 85 known for the specific sample, the combined product  $\varepsilon^{1/1} \omega_p$  is extracted as a  
 86 single parameter from the model and here-in the term 'plasma frequency' refers

87 to this product. The optical dispersion for the material, i.e. refractive index  $n$   
88 and extinction coefficient  $\kappa$ , is also extracted from the fitting procedure and the  
89 spectra are shown in the inset of figure 1.

90 Fitting was achieved by using a Nelder-Mead downhill simplex algorithm  
91 [13], implemented via python script, to minimize the quantity

$$\chi^2 = \sum_i^N \sqrt{\frac{y_i - O_i}{N^2}} \quad (2)$$

92 where  $N$  is the total number of data points in the spectra,  $O_i$  the observed  
93 transmittance at each wavelength over the range of interest, and  $y_i$  the the-  
94 oretical transmittance calculated using the transfer matrix method [14] for a  
95 single thin-film on a finite, transparent substrate. The fitting algorithm was it-  
96 erated until the relative fractional change in consecutive  $\chi^2$  values was less than  
97  $1 \times 10^{-6}$ . The fitting of all 289 transmittance spectra taken over the combina-  
98 torial sample was fully automated, the only user input required being an initial  
99 estimate of film thickness at the point of the first spectrum. This automation  
100 ensured that the fitting of consecutive spectra was highly consistent. For all  
101 spectra,  $\chi^2$  values of  $< 2$  were achieved indicating that all fits were as successful  
102 as that shown in figure 1.

103 It was not possible to extract values for the true optical band-gap  $E_G$  from  
104 the inter-band transition component of the model which relied on a simple  
105  $\alpha \propto (E - E_G)^{1/2}$  dependence to describe the behaviour in the vicinity of the  
106 band edge. All values of  $E_G$  were typically  $\sim 0.2 - 0.4$  eV lower than expected,  
107 even once non-parabolicity and re-normalisation effects had been accounted for,  
108 see sections 3.2 and 4). This is due to the presence of a population of impurity  
109 states located in energy just below the bottom of the conduction band. The  
110 presence of these states generates a broadening, commonly referred to as an  
111 ‘Urbach tail’ [15], in the onset of the absorption coefficient. It is very difficult  
112 to determine the extent of this broadening by fitting the dielectric model to a  
113 single transmittance spectra. The use of variable angle ellipsometry permitted  
114 a more reliable extraction of the band gap values due to the requirement that  
115 the fitting procedure satisfied multiple spectra simultaneously.

For each point over the combinatorial sample ellipsometric spectra were taken at angles of 65 and 70° with respect to a plane normal to the sample surface. The spectra were fitted using a parameterized semi-conductor (PSEMI-M0) model [16] over the range 350 – 1000 nm. Figure 2b shows a typical fit achieved by the model and the inset shows the difference in the  $\alpha^2$  versus  $E$  behaviour extracted from transmittance and ellipsometry data respectively. This disparity between band gaps extracted from the two techniques is in good agreement with that reported by Srikant [17] in ZnO.

### 3.2. Conduction band non-parabolicity

For highly doped metal-oxides it has been shown that the conduction band,  $E_c$ , is ‘non-parabolic’ and that the origin of this non-parabolicity may be attributed to a carrier dependent effective mass,  $m_e(n_e)$ . The functional form of this dependence, first suggested by Pisarkiewicz *et. al* [18], is given by

$$m_e(n_e) = m_{e0} \sqrt{1 + \frac{2C\hbar^2 k}{m_{e0}}} \quad (3)$$

where  $m_{e0}$  is the value of the effective mass at the conduction band minimum and  $C$  is the non-parabolicity factor, expressed in eV<sup>-1</sup>. The carrier wave-number can be expressed in terms of the carrier concentration according to  $k = (3\pi^2 n_e)^{1/3}$ . By re-examining equation 1 it is clear that the relationship between  $\omega_p^2$  and  $n_e$  becomes non-linear if the effective mass is not a constant. Figure 3 shows a plot of  $\omega_p$ , extracted from the spectrophotometry measurements, versus the carrier concentration,  $n_e^H$ , determined via Hall measurements, for the sample subset cut from the original combinatorial sample. A similar  $\chi^2$  minimization procedure to that described in section 3.1, in which the fitting parameters were  $m_{e0}$  and  $C$ , was applied to the data set using

$$\chi^2 = \sum_{i=1}^n \frac{(n_{e_i}^S - n_{e_i}^H)^2}{n^2} \quad (4)$$

where the superscript  $S$  corresponds to carrier concentrations calculated, using a carrier dependent effective mass  $m_e(n_e)$  (equations (1) and 3), from the

141 spectroscopically determined plasma frequencies. The superscript  $H$  denotes  
142 values of  $n_e$  determined directly from Hall measurements. To determine the  
143 uncertainty associated with the fitted  $m_{e0}$  and  $C$  values, Monte-Carlo style error  
144 treatment [19] was implemented within which the  $\chi^2$  minimization procedure  
145 was performed 1000 times. The inset plot in figure 3 shows the mean  $m_e(n_e)$   
146 relationship (solid line) and the corresponding spread (yellow line). An average  
147 extracted value of  $m_{e0} = 0.35 \pm 0.02 m_0$  is higher than previous published values  
148 of  $0.24 - 0.28 m_0$  for the effective mass in undoped ZnO. An average extracted  
149 value of  $C = 0.30 \pm 0.01$  eV agrees very well with previously reported values of  
150  $\sim 0.29$  eV<sup>-1</sup> [9, 20] for Al doped ZnO films.

### 151 3.3. Band-gap renormalization

152 The optical band gap of a degenerately doped metal-oxide system increases  
153 as a function of carrier concentration (Burstein-Moss shift [21, 22] according to

$$E_G = E_{G0} + \frac{\hbar^2(3\pi^2 n_e)^{2/3}}{2m_{JDOS}} \quad (5)$$

154 where  $E_{G0}$  is the band-gap at the conduction band minimum and the joint den-  
155 sity of states effective mass,  $m_{JDOS}$  is given as

$$\frac{1}{m_{JDOS}} = \frac{1}{m_h} + \frac{1}{m_e(n_e)} \quad (6)$$

156 A constant hole effective mass value of  $m_h = 0.7 m_0$  [23, 24] is assumed through-  
157 out this work. Note that the non-parabolicity of the conduction band is ac-  
158 counted for when estimating the band gap by the use of the carrier dependent  
159 effective mass  $m_e(n_e)$  determined in section 3.2. The data points in figure 4  
160 show the band-gap values, determined from ellipsometry, plotted against the  
161 Hall carrier concentrations. The points lie some distance from the relationship  
162 predicted by equation 5. The apparent reduction in the real band-gap values  
163 is due the re-normalization effects of many body electron-electron, electron-ion  
164 and electron-hole interactions. Lu *et. al* [25] have shown that the total energy  
165 shift due to re-normalization can be estimated by parameterising the detailed

166 model described by *Jain et. al* [26, 27] according to

$$E_R = An_e^{1/3} + Bn_e^{1/4} + Cn_e^{1/2} \quad (7)$$

167 where  $E_R$  is negative with respect to  $E_G$ . The  $n_e^{1/3}$ ,  $n_e^{1/4}$  and  $n_e^{1/2}$  dependencies  
 168 correspond to the exchange energy of free electrons, their correlation energy  
 169 and the electron-ion interaction energy respectively. The coefficients  $A$ ,  $B$ , and  
 170  $C$ , quantify the strength of each of these three dependencies. The coefficient  
 171 values and a value for  $E_{G0}$ , was extracted using the established minimisation  
 172 procedure. Table 1 shows the extracted values and comparative values for n-  
 173 type ZnO thin-films. The strength of the  $n_e^{1/3}$  dependence is roughly three times  
 174 than that reported for Al doped ZnO but vales for the other two coefficients are  
 175 consistent [25].

#### 176 4. Mapping of compositional dependence

177 Film thickness profiles were determined for the combinatorial ZnO:Si and  
 178 SiO<sub>2</sub> samples. The % wt. SiO<sub>2</sub> content at each point over the combinatorial  
 179 sample was estimated according to

$$x = \frac{\Gamma_B d_B}{\Gamma_A d_A + \Gamma_B d_B} \times 100\% \quad (8)$$

180 where  $\Gamma_A$  and  $\Gamma_B$  are the bulk densities of ZnO and SiO<sub>2</sub> respectively and  $d_A$  and  
 181  $d_B$  are the corresponding thicknesses,  $d$ , of the ZnO and SiO<sub>2</sub> films. The carrier  
 182 concentration profile for the combinatorial sample was calculated from extracted  
 183  $\varepsilon_\infty^{1/2} \omega_p$  values according to equation 1 and using the non-parabolic effective mass  
 184 relationship,  $m_e(n_e)$ , determined in section 3.2. The corresponding mobility  
 185 profile was calculated using

$$\mu_e = \frac{1}{n_e^S R_S d e} \quad (9)$$

186 where  $R_S$  are the sheet resistance values obtained directly from 4 point probe  
 187 measurements. Figure 5 shows the three dimensional contour profiles of  $n_e$  and  
 188  $\mu_e$  across the surface of the combinatorial sample. In both cases, a maximal  
 189 ridge, corresponding to  $n_e \sim 4.5 \times 10^{20} \text{ cm}^{-3}$  an  $\mu_e \sim 16 \text{ cm}^2 \text{V}^{-1} \text{s}^{-1}$ , runs



190 diagonally across the sample. By superimposing the contour distribution of  
 191 %, (dotted black contour lines), a very strong correlation between carrier con-  
 192 centration and composition becomes apparent, the maximum  $n_e$  and  $\mu_e$  values  
 193 corresponding to a value of  $x = 0.65\%$  and a minimum resistivity of  $8.6 \times 10^{-4}$   
 194  $\Omega\text{.cm}$ .

195 By plotting the distributions of  $n_e$  and  $\mu_e$  with respect to  $x$  the compositional  
 196 dependence can be observed directly as shown in figure 6. Here the strength  
 197 of the combinatorial analysis is fully appreciated by its ability to generate con-  
 198 tinuous, non-ambiguous distributions of the material's electrical behaviour and  
 199 shows that it is highly sensitive to the composition - the resistivity spanning  
 200 over three orders of magnitude within the compositional range  $x = 0 - 0.65\%$ .  
 201 Furthermore, the uncertainty in the optimum value of  $x$ , that minimises the  
 202 resistivity, is significantly reduced when compared to the multi-sample analyses  
 203 that are commonly reported.

204 The solid straight line in the  $n_e$  vs  $x$  plot indicates the relationship predicted  
 205 for a 100% doping efficiency, i.e. where every Si atom incorporated into film  
 206 substitutionally replaces a Zn atom and contributes two free electrons to the  
 207 system. For low values of  $x$ , i.e. in the range  $x = 0 - 0.5\%$ , this relationship  
 208 is adhered to. However as  $x$  increases further the doping efficiency decreases  
 209 rapidly and the carrier concentration is limited to  $3 - 4 \times 10 \text{ cm}^{-3}$  for com-  
 210 positions up to 10% wt.  $\text{SiO}_2$ . After the optimum value of  $x$  is reached, the  
 211 mobility drops off steeply and approaches a value of zero for values of  $x$  beyond  
 212 6%. This suggests that as  $x$  is increased beyond the optimum composition, Si  
 213 is incorporated interstitially rather than substitutionally or forming segregated  
 214 Si-) phases at the grain boundaries, thus acting to increase free carrier scattering  
 215 and so reducing mobility.

#### 216 4.1. Scattering

217 The behaviour of carrier mobility can be described further by considering  
 218 its direct relationship with the carrier concentration. Figure 7 shows that by  
 219 plotting  $\mu_e$  versus  $n_e$  for all data points in the range  $0 < x < 0.65\%$  a well de-

220 fined, unambiguous relationship is determined. The red data points correspond  
 221 to compositions  $x < 0.65\%$ . Within this distribution, and for carrier concen-  
 222 trations below  $2.5 \times 10 \text{ cm}^{-3}$  the mobility of the free carriers can be described  
 223 in terms of the grain barrier limited transport model proposed by Seto *et.al*  
 224 [28]. The model assumes that at the grain boundaries a population of filled  
 225 and charged trap states exists within the band gap. This causes the conduc-  
 226 tion band to bend upwards at each grain boundary forming a barrier to charge  
 227 transport. The inter-grain mobility,  $\mu_B$  of free carriers is therefore limited by  
 228 thermal processes according to

$$\mu_{ig} = \mu_0 \exp\left(-\frac{\Phi_B}{k_B T}\right) \quad (10)$$

229 where  $\Phi_B$  is the barrier height at the grain boundary and is related directly to  
 230 the carrier concentration according to

$$\Phi_B = \frac{e^2 n_t}{8\varepsilon_\infty \varepsilon_0 n_e} \quad (11)$$

231 where  $n_t$  is the trap density. The pre-factor  $\mu_0$  is the internal mobility of the  
 232 grain, expressed as

$$\mu_0 = \frac{eL}{\sqrt{2\pi m_e k_B T}} \quad (12)$$

233 where  $L$  is the grain size. It is necessary to extend the Seto model in the case  
 234 of degenerately doped ZnO to account for the tunnelling of carriers through  
 235 the barrier  $\Phi_B$ . As the carrier concentration increases the Fermi level rises  
 236 towards the top of the barrier while the barrier height decreases proportionally  
 237 to  $1/n_e$ . Following the onset of tunnelling the effective carrier mobility increases  
 238 exponentially with respect to carrier concentration. The increase in mobility is  
 239 eventually limited by other scattering processes, for example ionized-impurity  
 240 scattering. A semi-empirical relationship the mobility due to the tunnelling of  
 241 free carriers,  $\mu_t$  can be expressed according to

$$\mu_t = \frac{\mu_{ii} - \mu_{ig}}{1 + \exp\left[-\frac{1}{\alpha}(\Delta_{BM} + E_R - \beta\Phi_B)\right]} \quad (13)$$

242 where the factor  $\alpha$  accounts for the sharpness of the onset in tunnelling and  
 243 is likely to be related to the depletion width of the grain boundary. A second

empirical factor,  $\beta$  approximates any extra functional dependence of  $\Phi_B$  on  $n_t$  which is likely vary with respect to  $n_e$ . The effective mobility may therefore be expressed as the sum of the inter-grain and tunnel mobilities according to

$$\mu_{eff} = \mu_{ig} + \mu_t \quad (14)$$

Figure 7 shows the corresponding the fit of this extended model to the data. An extracted value of  $n_t = 1.79 \times 10^{14} \text{ cm}^{-3}$  is over two orders of magnitude greater than that reported for reactively sputtered, undoped ZnO films [29] and an order of magnitude greater than that for Al doped ZnO films [30]. This is reflected in the relatively low optimum mobility values of  $\sim 16 \text{ cm}^2\text{V}^{-1}\text{s}^{-1}$  which is typically half that of Al doped ZnO films. The reduction of the trap densities at the grain boundaries is therefore key to the improvement of carrier mobility in Si doped ZnO films. This is likely to be achieved through further investigations of the effect of growth parameters, i.e. substrate temperature and sputter pressure. Based on the model used in this work, a reduction of  $n_t$  by  $\sim 20\%$  could yield a doubling of the mobility.

## 5. Conclusions

A consideration of the non-parabolicity of the conduction band for Si doped ZnO has yeilded estimates for the values of the band minimum effective mass,  $m_{e0} = 0.35m_0$ , and the non-parabolicity factor,  $C = 0.3 \text{ eV}^{-1}$ . The non-parabolicity contributes to a reduction in the expected Burstein-Moss shift of the optical band-gap at carrier concentrations beyond  $10^{20} \text{ cm}^{-3}$ . Further reductions in the band-gap arises from the renormalization effects which are dominated by electron-electron and electron-ion interactions. For Si doped films the component of the magnitude of these effects are significantly greater than that reported for sputtered Al doped ZnO films.

The combinatorial methodology employed within this work allows the relationship between composition and the electrical behaviour to be determined with excellent accuracy, with a continuous distributions between  $n_e$ ,  $\mu_e$ ,  $\rho$  and

271 % wt. SiO<sub>2</sub> being determined. Furthermore, the extraction of all data from a  
 272 single sample ensures that a high level of consistency between each data point  
 273 is achieved compared with measurements taken over a series of separately de-  
 274 posited samples. Maximum values of  $4.5 \times 10^{20} \text{ cm}^{-3}$  and  $16 \text{ cm}^2\text{V}^{-1}\text{s}^{-1}$  were  
 275 achieved for the carrier concentration and mobility respectively, at an optimal  
 276 composition of  $x = 0.65\%$  wt. SiO<sub>2</sub>, and this corresponding to a minimum  
 277 resistivity of  $8.7 \times 10^{-4} \Omega\text{.cm}$ .

278 The model of grain boundary scattering proposed by *Seto* [28] has been  
 279 extended to include the effects of tunneling through grain boundaries. The  
 280 model generates a good agreement for the observed  $\mu_e$  versus  $n_e$  behaviour at  
 281 compositions up to the optimum value of  $x$ . The model highlights a potential  
 282 route to improving carrier mobility, i.e. by reducing the density of trap states  
 283 that exist at the grain boundaries.

284 Above the optimum composition a different dependence is observed to that  
 285 below it. This is thought to be due to the increased density of trap states  
 286 associated with the incorporation of excess Si into the films.

## 287 Acknowledgements

288 The authors are grateful to Dr. Tim Veal for useful discussions concerning  
 289 the work and to Vincent Vasey for technical assistance. This work was funded  
 290 by EPSRC, grant number EP/F029624 and and EP/K018884/1.

## 291 References

- 292 [1] T. Minami, *Semicond. Sci. Technol.* 20 (2005) S35.
- 293 [2] J. Hu, R. Gordon, *Solar Cells* 30 (1991) 437–450.
- 294 [3] R. E. Treharne, K. Durose, *Thin Solid Films* 519 (2010) 7579–7582.
- 295 [4] J. Rousset, E. Saucedo, D. Lincot, *Chem. Mater.* 21 (2009) 534–540.

- [5] P. R. Chalker, P. A. Marshall, S. Romani, J. Roberts, W. Joseph, S. J. C. Irvine, D. Lamb, A. Clayton, J. Andrew, P. A. Williams, J. Vac. Sci. Technol. A 31 (2012) 01A120–01A120.
- [6] S. Y. Myong, S. J. Baik, C. H. Lee, W. Y. Cho, K. S. Lim, Jpn. J. Appl. Phys. 36 (1997) L1078.
- [7] S.-M. Park, T. Ikegami, K. Ebihara, S.-M. Shin, Paik-Kyun Park, T. Ikegami, K. Ebihara, P.-K. Shin, App. Surf. Sci. 253 (2006) 1522–1527.
- [8] T. Minami, T. Miyata, Y. Ohtani, Y. Mochizuki, Jpn. J. App. Phys. 45 (2006) L409–L412.
- [9] K. Ellmer, J. Phys. D: Appl. Phys 34 (2001) 3097–3108.
- [10] R. E. Treharne, K. Hutchings, D. A. Lamb, S. J. C. Irvine, D. Lane, K. Durose, J. Phys. D: Appl. Phys 45 (2012) 335102.
- [11] D. Mergel, Z. Qiao, J. Phys. D: Appl. Phys 35 (2002) 794.
- [12] N. Ashkenov, B. N. Mbenkum, C. Bundesmann, V. Riede, M. Lorenz, D. Spemann, E. M. Kaidashev, A. Kasic, M. Schubert, M. Grundmann, J. Appl. Phys. 93 (2003) 126–133.
- [13] J. A. Nelder, R. Mead, The Computer Journal 7 (1965) 308–313.
- [14] H. A. Macleod, Thin-Film Optical Filters, Adam Hilger Ltd, 1986.
- [15] F. Urbach, Phys. Rev. 92 (1953) 1324.
- [16] C. Herzinger, B. Johs, W. McGahan, J. Woollam, W. Paulson, J. Appl. Phys. 83 (1998) 3323–3336.
- [17] V. Srikant, D. R. Clarke, J. Appl. Phys. 83 (1998) 5447–5451.
- [18] T. Pisarkiewicz, A. Kolodziej, Phys. Stat. Sol. B 158 (1990) K5–K8.
- [19] R. J. Mendelsberg, Photoluminescence of ZnO grown by eclipse pulsed laser deposition, Ph.D. thesis, University of Canterbury, New Zealand, 2009.

- 321 [20] F. Ruske, A. Pflug, V. Sittinger, B. Szyszka, D. Greiner, B. Rech, Thin  
322 Solid Films 518 (2009) 1289–1293. Article in press - Thin Solid Films.
- 323 [21] E. Burstein, Phys. Rev. 93 (1954) 632–633.
- 324 [22] T. S. Moss, Proc. Phys. Soc. B 67 (1954) 775.
- 325 [23] G. Beni, T. Rice, Phys. Rev. B 18 (1978) 768.
- 326 [24] D. C. Reynolds, D. C. Look, B. Jogai, Solid State Comm. 99 (1996) 873–  
327 875.
- 328 [25] J. Lu, S. Fujita, T. Kawaharamura, H. Nishinaka, Y. Kamada, T. Ohshima,  
329 Z. Ye, Y. Zeng, Y. Zhang, L. Zhu, et al., J. Appl. Phys. 101 (2007) 083705–  
330 083705.
- 331 [26] S. Jain, J. McGregor, D. Roulston, J. Appl. Phys. 68 (1990) 3747–3749.
- 332 [27] S. C. Jain, D. J. Roulston, Sol. State. Elec. 34 (1991) 453–465.
- 333 [28] J. Y. W. Seto, J. Appl. Phys. 46 (1975) 5247–5254.
- 334 [29] P. F. Carcia, R. S. McLean, M. H. Reilly, G. Nunes, App. Phys. Lett. 82  
335 (2003) 1117–1119.
- 336 [30] M. Kon, P. Song, Y. Shigesato, P. Frach, S. Ohno, K. Suzuki, Jpn. J. App.  
337 Phys. 42 (2003) 263–269.
- 338 [31] B. Johs, J. A. Woollam, C. M. Herzinger, J. Hilfiker, R. Synowicki, C. L.  
339 Bungay, Crit. Rev. Opt. Sci. CR72 (1999) 29–58.
- 340 [32] R. J. Mendelsberg, Y. Zhu, A. Anders, J. Phys. D: Appl. Phys 45 (2012)  
341 425302.

Parameter 1	Extracted Value	Copmparison [25]
$A (\times 10^{-8} \text{ eV.cm})$	$2.1 \pm 0.8$	0.69
$B (\times 10^{-7} \text{ eV.cm}^{3/2})$	$3.0 \pm 2.6$	1.6
$C (\times 10^{-7} \text{ eV.cm}^{3/4})$	$8.7 \pm 1.5$	7.76
$E_{G0} \text{ (eV)}$	$3.41 \pm 0.01$	-

Table 1: Parameter values extracted from the downhill-simplex fit of equation 7 to the experimental data shown in figure 4.  $E_G$  values were extracted from fits to ellipsometry spectra taken in the vicinity of the band gap and  $n_e$  values were determined by Hall measurements. The coefficients A, B and C correspond to the amplitudes of the separate  $n_e^{1/3}$ ,  $n_e^{1/4}$ ,  $n_e^{1/2}$  dependencies respectively of the renormalisation effects.

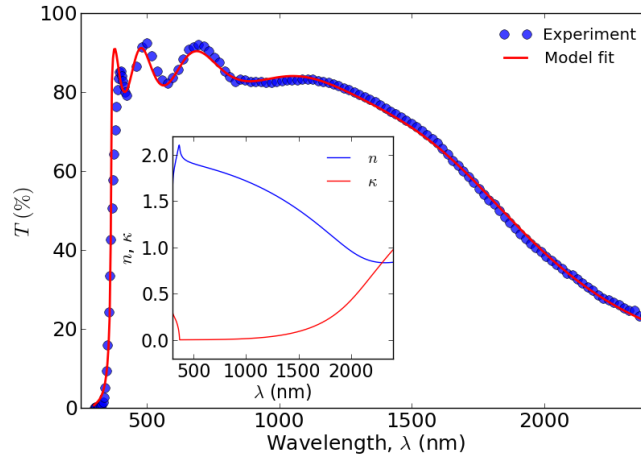


Figure 1: Example of a typical transmittance curve taken from a single point on the combinatorial ZnO:Si sample. The line (—) shows the corresponding fit generated by the dielectric model [10]. An excellent fit is achieved at wavelengths in the vicinity of plasma edge, i.e.  $\lambda > 1000 \text{ nm}$ . The band to band transition component of the model is insufficient to accurately describe the behaviour in the vicinity of the material's direct band gap. In this instance, values of  $d = 518 \pm 10 \text{ nm}$ ,  $\varepsilon_{\infty}\omega_p = 0.97 \pm 0.02 \text{ eV}$  and  $E_G = 3.38 \pm 0.04 \text{ eV}$  were extracted from the fitting procedure. The inset also shows the dispersion relationships for  $n$  and  $\kappa$  extracted by the model.

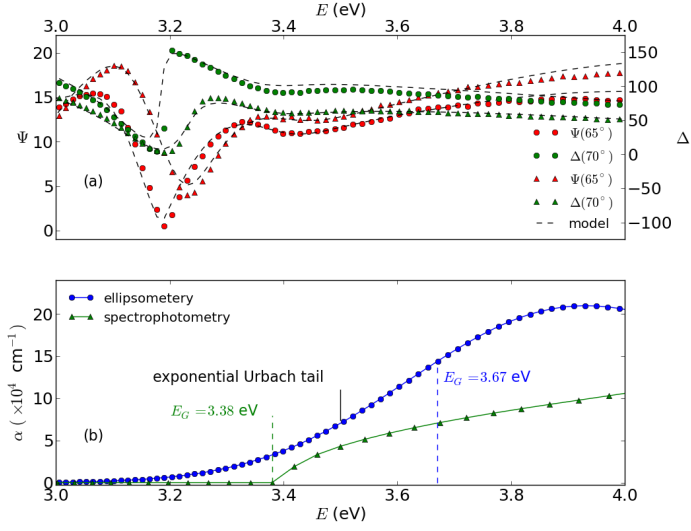


Figure 2: a) Ellipsometric spectra ( $\Psi$  and  $\Delta$ ), measured at separate angles of  $65^\circ$  and  $70^\circ$ , were fitted over the range 3 eV (413 nm) to 4 eV (309 nm) using a single PSEMI-M0 oscillator [16, 31], b) The corresponding absorption coefficient extracted from the ellipsometric data compared with that extracted from the spectrophotometric data (1). A difference in the direct band gap of  $\sim 0.3$  eV is determined between the two optical extraction methods. The ellipsometric model is deemed to be more reliable due to its ability to account for the Urbach tail that arises from a distribution of impurity states located just below the bottom of the conduction band.



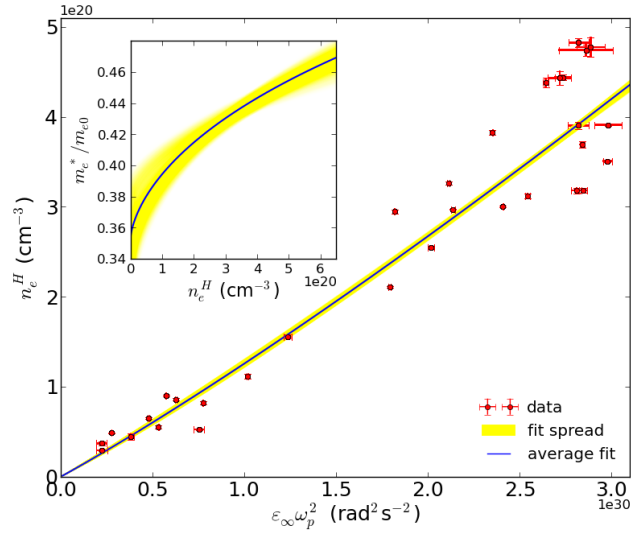


Figure 3: Carrier concentration,  $n_e^H$ , determined via Hall effect measurements versus values of  $(\epsilon_\infty \omega_p)^2$  extracted from the dielectric modeling of transmittance data. A Monte-Carlo style fitting procedure [19, 32] indicates that the relationship between the axes is non-linear, as expected for a material with a non-parabolic conduction band. The spread in uncertainty associated with the fitting procedure is shown by the yellow line. The corresponding relationship between the carrier effective mass,  $m_e$  and the carrier concentration is shown in the inset. Values of  $m_{e0} = 0.35 \pm 0.02 m_0$  and  $C = 0.30 \pm 0.01 \text{ eV}^{-1}$  were extracted from the analysis.

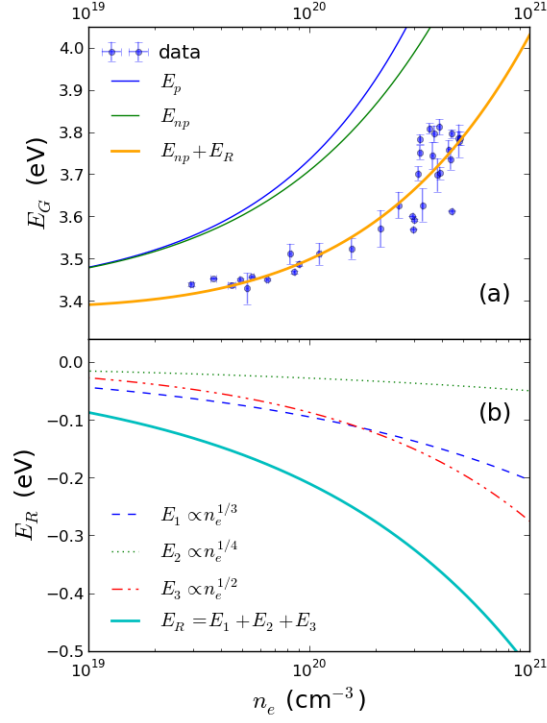


Figure 4: a) Ellipsometry extracted band gap values,  $E_G$ , plotted with respect to the carrier concentration determined by Hall measurements. The Burstein-Moss relation ( $E_p$ ), even once non-parabolicity is accounted for ( $E_{np}$ ), is insufficient to predict the observed relationship - band gap values being significantly lower than expected. The incorporation of renormalization effects permits the data to be fitted. b) The total renormalization energy and each of its subcomponents are shown. The amplitude of these components is calculated empirically via a Monte-Carlo fitting procedure using the model proposed by [26].

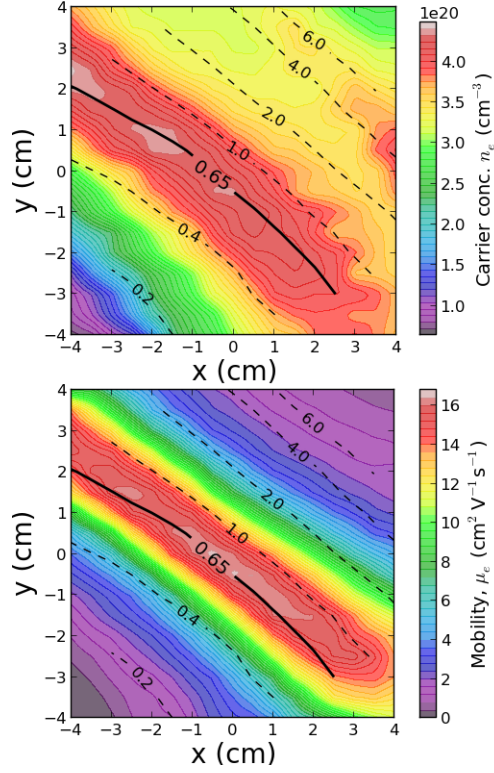


Figure 5: 3D contour plots of the carrier concentration and mobility over the combinatorial sample. All values were extracted using the automated spectrophotometric mapping procedure. The ( - - ) contour lines show an overlay of the % wt.  $\text{SiO}_2$  composition.

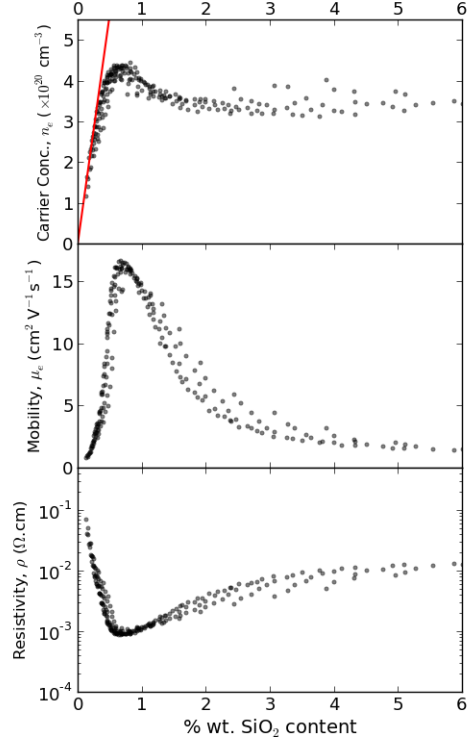


Figure 6: Distributions of carrier concentration, mobility and resistivity with respect to % wt.  $\text{SiO}_2$  content. The maximum values for  $n_e$  ( $4.4 \times 10^{20} \text{ cm}^{-3}$ ) and  $\mu_e$  ( $16.5 \text{ cm}^2 \text{V}^{-1} \text{s}^{-1}$ ) coincide with a composition of 0.65% wt.  $\text{SiO}_2$  and correspond to a minimum resistivity of  $8.6 \text{ } \Omega \cdot \text{cm}$ . The solid straight line (—) in the top plot shows the maximum theoretical carrier concentration achievable if every Si atom incorporated onto a zinc site contributes two free electrons to the system.

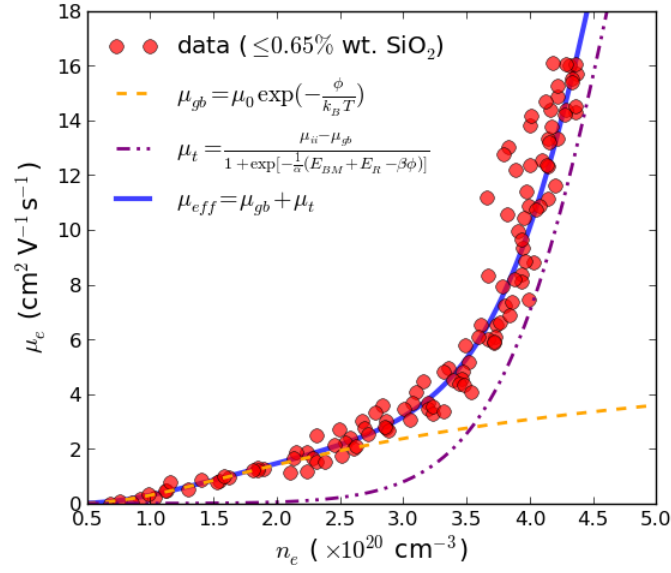


Figure 7: Relationship between  $n_e$  and  $\mu_e$  values extracted from the automated spectrophotometric mapping procedure. All data points have compositions below and up to the optimum value of 0.65% wt.  $\text{SiO}_2$ . The line (—) shows the fit achieved to the data using equations 10-14. The parameter values  $n_t = 1.7 \times 10^{14} \text{ cm}^2$ ,  $L = 40 \text{ nm}$ ,  $\alpha = 25 \text{ eV}$  and  $\beta = 0.54$  were extracted from a downhill-simplex fitting procedure [13]. An estimated value of  $\mu_{ii} = 40 \text{ cm}^2\text{V}^{-1}\text{s}^{-1}$  was chosen for the fitting but the extracted values were shown to be relatively independent of  $\mu_{ii}$  in the range  $20 - 100 \text{ cm}^2\text{V}^{-1}\text{s}^{-1}$ .